Estimating fractured rock effective permeability using discrete fracture networks constrained by electrical resistivity data

Jin Wu [a], Tada-nori Goto [b],[*], Katsuaki Koike [a]

[a] Department of Urban Management, Graduate School of Engineering, Kyoto University, Katsura, Kyoto 615-8540, Japan
[b] Graduate School of Science, University of Hyogo, Himeji, Hyogo 671-2280, Japan

ARTICLE INFO

ABSTRACT

Although the permeability of fractured rock mass is a fundamentally important property for the safe construction of civil and mining engineering structures such as tunnels, in situ characterization of permeability without resorting to hydraulic tests is difficult. For rapid, wide-area estimation, a method that can be conducted at a field-scale using geological and geophysical investigation data is proposed. The method is not based on conventional hydraulic test results. Instead, it combines the stochastic generation of fracture networks with the crack tensor theory. The most important parameter for this method is the fracture length distribution. Although the distribution parameters in the DFN model are assigned through sampling, a bias is generally experienced because of the limited sampling area. To improve the estimation of such parameters, in-situ electrical resistivity data and a symmetric self-consistent method are used to constrain the fracture length distribution. The proposed method is applied to the fractured crystalline rock mass of the Mizunami Underground Research Laboratory (URL) in the Tono area of central Japan. Its effectiveness and correctness are demonstrated through good correspondence of the derived effective permeability with the in-situ measured permeability.

List of symbols

a	scaling exponent
b	fracture aperture (m)
f	empirical connectivity parameter
g	gravitational acceleration (m/s^2)
$\bar{k}$	average permeability (m^2)
k_{ij}	permeability (m^2)
l	fracture length (m)
l_{min}	minimum fracture size (m)
l_{max}	maximum fracture size (m)
n	unit vector of normal orientation for a fracture
$n(l)$	number of fractures with sizes in the range $[l, l + dl]$ per unit of volume (m^{-3})
r	fracture radius (m)
D	fracture diameter (m)
K_{ij}	Hydraulic conductivity (m/s)
L	characteristic size (m)

M_{ij}	basic quantity for Oda's crack tensor theory
N	number of fractures or fracture sets
$N(l, L)$	total fracture number with sizes in the range $[l, l + dl]$ in a volume of characteristic size L
P_{10}	number of fractures per unit length (m^{-1})
P_{32}	cumulative surface of fracture per unit volume (m^{-1})
V_e	grid block volume (m^3)
γ	fracture density term
δ_{ij}	Kronecker's delta
ε	dimensionless fracture density
ζ	number of fractures per volume (m^{-3})
θ	standard deviation of a Fisher Distribution
κ	Fisher constant or dispersion factor
μ	water viscosity (Pa • s)
τ	mean number of intersections per fracture
τ_c, β	parameter used in the improved Oda's crack tensor theory
$\bar{\rho}$	average electrical resistivity (Ωm)

* Corresponding author.
 E-mail addresses: jin.alex.wu@hotmail.com (J. Wu), t.n.goto@sci.u-hyogo.ac.jp (T-n Goto), koike.katsuaki.5x@kyoto-u.ac.jp (K. Koike).

ρ_{ij}	effective electrical resistivity (Ωm)
ρ_w	water density (kg/m³)
$\widetilde{\sigma}_{ij}$	effective electrical conductivity (S/m)
σ_f	fracture electrical conductivity (S/m)
σ_m	matrix electrical conductivity (S/m)
ω	aspect ratio

1. Introduction

Fractures (e.g., joints, faults), which are geologic discontinuities, are ubiquitous at different length scales in crustal rocks: they can extend for millimeters to kilometers. Fractures are fundamentally important for engineering applications such as high-level radioactive waste disposal, enhanced geothermal systems, and underground construction because they might serve as pathways of fluid flow or barriers that prevent flow across them (e.g., Ishibashi et al., 2016; Li et al., 2009; Wolfsberg, 1996). Especially at excavations of underground tunnels in hard-rock masses, highly pressurized groundwater inflow in fractures causes geohazards (e.g., Li et al., 2009). Estimating the permeability of fractured rock masses persists as a challenging issue for studying fluid flow and transport behaviors in fractured rock masses. Permeability can exist as equivalent or effective permeability. The latter, an intrinsic rock property at a large homogenization scale with a representative elementary volume (REV) size (Lei et al., 2017; Renard and De Marsily, 1997), is the main target of this study.

Generally, permeability can be measured using laboratory tests, field tests within boreholes, and numerically based upscaling algorithms (e.g., Sævik and Nixon, 2017). Field hydraulic tests using packers and water pumps in single or multiple boreholes are more reliable than laboratory tests for estimating the field-scale effective permeability of fractured rock mass over a size larger than REV (Hamm et al., 2007). Multiple-borehole hydraulic tests are used for measuring anisotropic permeability if the fractured rock is assumed homogeneous and anisotropic.

Typical difficulties hindering the use of such hydraulic tests are the high cost and the necessity of long experimental times (Wolfsberg, 1996). Numerical and analytical methods have been developed to characterize the main fractures hydraulically and to estimate permeability. Fluid flow and transport through fractured rock mass can be modeled using the Equivalent Continuum (EC), the Discrete Fracture-Matrix (DFM) model, Discrete Fracture Network (DFN), and Pipe Network (PN, e.g., Dershowitz and Fidelibus, 1999; Hadgu et al., 2017; Koike et al., 2015; Leung et al., 2012; Liu et al., 2019). The EC models are based on dual porosity (Barenblatt et al., 1960; Warren and Root, 1963), dual permeability (Vogel et al., 2000), and multi-continuum method (Pruess and Narasimhan, 1982; Pruess et al., 1999). However, EC models are inappropriate to simulate the fluid flow through a small number of large-scale fractures. A DFM model, which uses two-point or multi-point flux approximations to assess interactions between a rock matrix and fractures, has been well developed to model fluid flow in fractured rock masses (Karimi-Fard et al., 2003; Sandve et al., 2012). For cases in which fractures provide predominant pathways of fluid flow in a rock mass with low permeability, a DFN model or a pipe network model is reliable (e.g., Valera et al., 2017).

Those numerically based methods engender requirements for high computational demand. Therefore, analytical methods such as the crack tensor theory (e.g., Oda, 1986) are applicable as alternatives. Analytical models might also use stochastically generated fracture DFNs. An important difficulty of DFN modeling is the incorrectness of the fracture length distribution that is inferred from the trace lengths obtained from outcrops and tunnel walls (Mak, 2014). Several simplifications are necessary for estimation of the distribution parameters, which might cause unrealistic DFN. Therefore, rational constraints are necessary for correction of the fracture length distribution. Although geophysical, hydrological, and geomechanical data have been used as constraints for stochastic DFN modeling (den Boer and Sayers, 2018; Dorn et al., 2013; Follin et al., 2014; Lei et al., 2014; Williams-Stroud et al., 2013), no method using electrical resistivity data has been proposed for constraining the fracture length distribution.

Herein, the electrical resistivity is selected as a novel constraint condition of a DFN because it is sensitive to permeable fractures through which much of the groundwater flows. The primary objective of this study is to estimate the effective permeability accurately and efficiently without hydraulic tests by combining DFN modeling and a crack tensor theory with a constraint by in-situ measured resistivity for fracture length distribution and upscaling of calculated permeability. The resistivity data used for this study originate from geological surveys conducted with borehole cameras and geophysical logging in a pilot borehole for tunnel excavation (Fig. 1). The constrained DFN model is then used to estimate upscaled permeability. The proposed method is applied to the fractured crystalline rock mass of the Mizunami Underground Research Laboratory in the Tono area of central Japan as a case study. Its effectiveness is demonstrated by comparing the estimated effective permeability with the in-situ measured permeability. This paper is organized as follows. Section 2 introduces the DFN modeling approach, Oda's crack tensor theory and symmetric self-consistent method. Then, an overall workflow is presented in Fig. 2. Finally, two cases studies are conducted to validate our proposed method.

2. Methods for calculating effective permeability

2.1. Discrete fracture network modeling

The first step is DFN modeling of fracture distribution because exact deterministic expression of fractures using limited field survey data from outcrops and scanlines is impossible. The DFN modeling expresses stochastic fracture properties such as fracture locations, shapes, lengths, orientations, and apertures and their correlations. Following
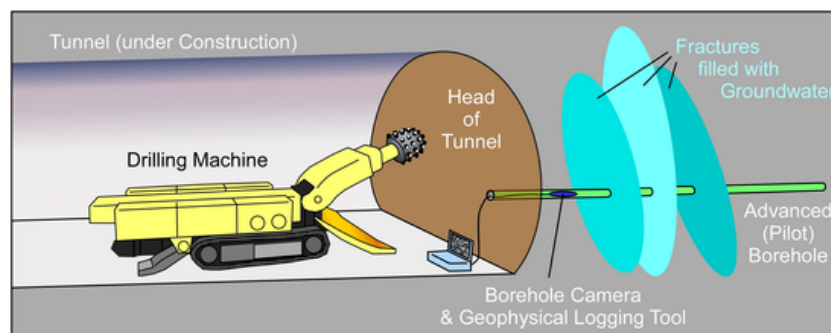

Fig. 1. Schematic view of an advanced (pilot) borehole. Camera and logging tools (e.g., electrical logging) are installed along an advanced hole.
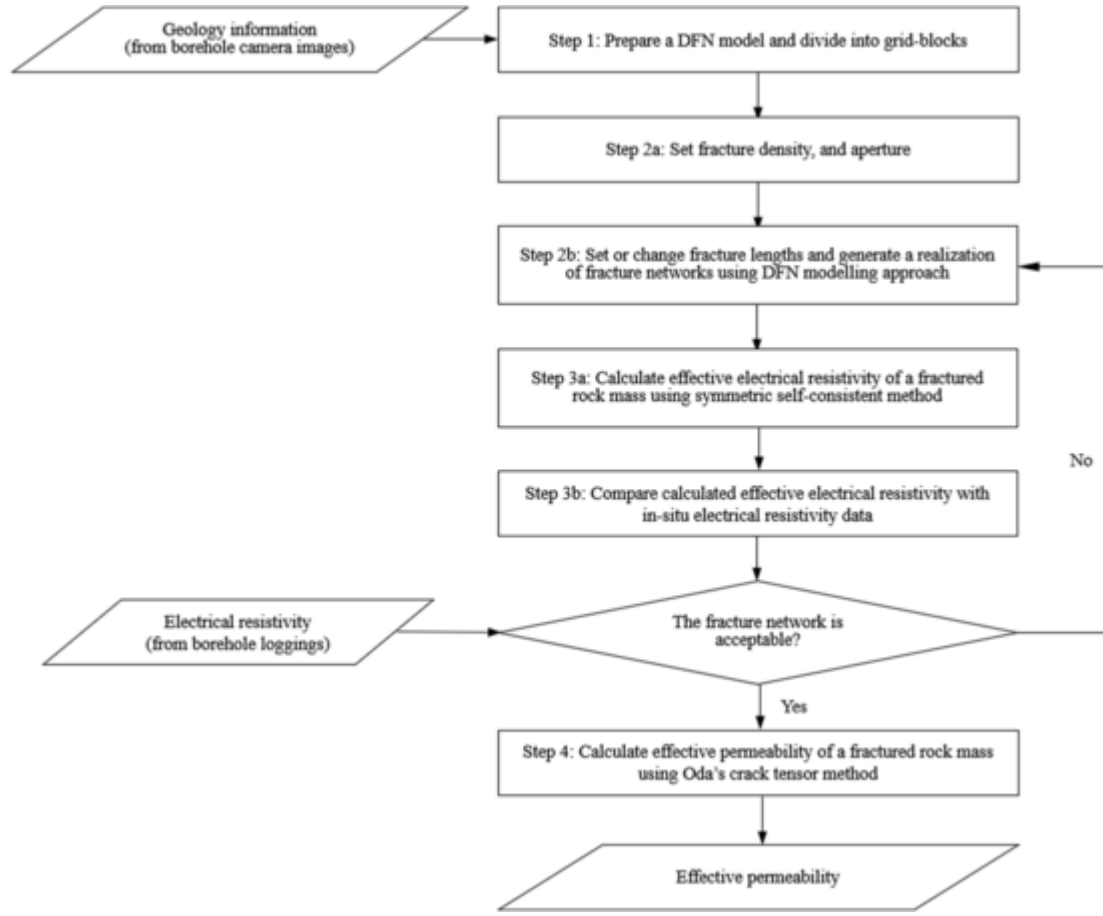
Fig. 2. Flowchart for calculating field-scale effective permeability of a fractured rock mass by combining the DFN model with the improved Oda's crack tensor with a constraint by in-situ measured resistivity data for the fracture length distribution.

traditional DFN modeling, this study adopted a homogeneous Poisson approach for fracture position (Xu and Dowd, 2010). This process is based on a random process controlled by a scale-averaging fracture density such as P_{10} or P_{32} in space (Dershowitz and Einstein, 1988). Actually, P_{32} is a scale-averaging volumetric measure of fracture intensity by the total fracture surface area per unit volume; P_{10} is the number of fractures per unit length. Because P_{32} cannot be estimated directly, it is derived from P_{10} using an analytical or a numerical method.

Fracture orientations were derived from the dip direction and angle data that were assumed to follow the von Mises–Fisher distribution with the following probability density function $f(\theta)$ as:

$$f(\theta) = \frac{\kappa \sin \theta e^{\kappa \cos \theta}}{e^{\kappa} - e^{-\kappa}} \tag{1}$$

where θ (°) stands for the standard deviation of the dip direction and angle and κ is a Fisher constant expressing dispersion of direction clusters. When κ is large, fractures are closely and parallelly distributed. Fracture orientations can be described as a Fisher distribution for $\kappa \geq 5$.

Fracture length distribution is usually derived from observed trace lengths and is assumed to follow a truncated power law by defining the minimum and maximum lengths (l_{min} and l_{max}) (Lei et al., 2017). A fracture size density distribution, $n(l)$, which describes the number of fractures per unit of volume in the range $[l, l + dl]$ ($dl \ll l$), is used to set the fracture length distribution as shown below:

$$n(l) = \gamma l^{-a}, l \in [l_{\min}, l_{\max}] \tag{2}$$

In that equation, γ is a fracture density term and a is a scaling exponent. The total number of fractures with sizes in the range of $[l, l + dl]$ in a volume of characteristic size L, $N(l, L)$, is equal to the following:

$$N(l, L) = n(l) L^3 dl \tag{3}$$

If a computational domain is cubic, then L is the cube side length. It is noteworthy that L should be larger than or equal to the REV size. For the 3D space, γ is equal to P_{32} and $a \geq 2$ (Lei et al., 2017). A fundamentally important difficulty is how to find an unknown a value correctly. Assuming that rock mass is saturated, the total volume of saturated fractures is proportional to the total length of fractures in the range $[l_{min}, l_{max}]$. Also, the fracture apertures are constant. In situ measured resistivity data were used to find a, as described in Section 2.3.

The fracture aperture has been regarded as correlated with the fracture length. Its distribution is generally approximated as a power law or a lognormal distribution (Lei et al., 2017; Min et al., 2004). The uniform assumption is for cases without sufficient aperture data by observation.

2.2. Crack tensor theory

As a semi-analytical upscaling method to calculate the effective permeability of a fractured rock mass, Oda's crack tensor theory has been used widely by assuming the fracture shape as a penny disk (e.g., Koike et al., 2012; Oda, 1986). By defining the position, size, and orientation of each disk, a quantity of fractures intersecting a block with volume V_e larger than REV, M_{ij}, can be expressed as the following:

$$M_{ij} = \frac{1}{V_e} \frac{\pi}{4} D^2 b^3 n_i n_j \tag{4}$$

Therein, D, b, and $n_i (i = 1,2,3)$, respectively represent the diameter, aperture, and the unit vector component of normal orientation of the fracture disk. The permeability k_{ij} (m^2) of V_e is then calculated using a discrete crack tensor approach (Rutqvist et al., 2013; Wang et al., 2014) as the following equation:

$$k_{ij} = \sum_{i=1}^{N} \frac{1}{12} \left(M_{kk} \delta_{ij} - M_{ij} \right) \tag{5}$$

In that equation, the so-called Oda's crack tensor theory, N represents the total number of fractures intersecting V_e; δ_{ij} is Kronecker's delta.

To avoid overestimation of fracture connectivity, an empirical connectivity parameter f for fractures that contribute considerably to effective permeability was introduced as shown below:

$$k_{ij} = \sum_{i=1}^{N} f \left(M_{kk} \delta_{ij} - M_{ij} \right) \tag{6}$$

In addition, f was given concretely as (Mourzenko et al., 2011):

$$f = \begin{cases} \frac{(\tau - \tau_c)^2}{\tau(1/\beta + \tau - \tau_c)}, \tau' \geq \tau_c \\ 0, \tau' < \tau_c \end{cases} \tag{7}$$

where τ represents the mean number of intersections per fracture and τ_c stands for the percolation threshold. Eqs. (6) and (7) are the improved Oda's crack tensor theory, used in this study. Condition $\tau < \tau_c$ is for a disconnected fracture network; fracture permeability $= 0$. The combination of $\tau_c = 2.41$ and $\beta = 0.18$ is for the disk-shaped fracture set (Mourzenko et al., 2011; Sævik et al., 2013) used for this study.

The permeability tensor in the 3D space is expressed as shown below:

$$k_{ij} = \begin{bmatrix} k_{xx} & k_{xy} & k_{xz} \\ k_{yx} & k_{yy} & k_{yz} \\ k_{zx} & k_{zy} & k_{zz} \end{bmatrix}$$

Therein, $k_{xy} = k_{yx}$, $k_{xz} = k_{zx}$ and $k_{yz} = k_{zy}$ for a symmetric second-order tensor. Average effective permeability $\bar{k}$, the main rock-mass property of this study, is the average of diagonal components (Li et al., 2009) as presented below:

$$\bar{k} = \frac{1}{3} \left(k_{xx} + k_{yy} + k_{zz} \right) \tag{8}$$

2.3. Symmetric self-consistent method

Because the resistivity of rock mass is sensitive to the existence of fractures, in-situ measured resistivity data by geophysical logging in a pilot borehole before tunnel excavation are useful to constrain a DFN model, particularly the fracture length distribution. For this constraint, close matching between the calculated and measured resistivity of rock mass is indispensable. The symmetric self-consistent method (SSC; Sævik et al., 2013, 2014) for upscaling effective resistivity ρ_{ij} from resistivity data was used for this matching, because it can consider fracture interactions under large fracture density. In a homogeneous medium of matrix conductivity σ_m (inverse of resistivity) with N conductive fractures, ρ_{ij} is formulated as:

$$\rho_{ij} = \frac{1}{\tilde{\sigma}_{ij} \sigma_m} \tag{9}$$

$$\tilde{\sigma}_{ij} = \delta_{ij} + \frac{1}{3} \sum_{k=1}^{N} \frac{\varepsilon_k (2\alpha + 1)}{\lambda_k \alpha + \frac{\pi}{4}} \left(\delta_{ij} - n_i n_j \right) \tag{10}$$

where the following are true:

$$\alpha = 1 + \frac{2}{9} \sum_{k=1}^{N} \frac{\varepsilon_k (2\alpha + 1)}{\lambda_k \alpha + \frac{\pi}{4}} \tag{11}$$

$$\varepsilon = \frac{4}{3} \pi \zeta r^3 \tag{12}$$

$$\lambda = \frac{\sigma_m}{\sigma_f \omega} \tag{13}$$

In those equations, ε represents the dimensionless fracture density, ζ denotes the number of fractures per unit volume, r stands for the fracture radius, σ_f denotes conductivity of saturated fracture, and ω expresses the fracture aspect ratio of aperture divided by diameter, $\sigma_f \omega$ requires corrections for converge. Similarly to $\bar{k}$, average resistivity $\bar{\rho}$ is given by calculating the diagonal components of ρ_{ij} as shown below:

$$\bar{\rho} = \frac{1}{3} \left(\rho_{xx} + \rho_{yy} + \rho_{zz} \right) \tag{14}$$

2.4. Analytical flow

Estimation of $\bar{k}$ of a fractured rock mass was implemented along the flow chart in Fig. 2. The first step is construction of a DFN model using fracture data for orientation and density from borehole camera images and a truncated power law of the fracture length distribution.

The second step is calculation of $\bar{\rho}$ from the DFN model using SSC and comparison of $\bar{\rho}$ with the average of in-situ resistivity data from borehole loggings. If the difference is large, then the DFN model is modified by changing the a value in Eq. (2). Otherwise $\bar{k}$ is calculated finally using the improved Oda's crack tensor.

3. Application to field data

3.1. Study site and fracture data

The proposed method was applied to permeability characterization of a part of the Mizunami Underground Research Laboratory (MIU) in Gifu Prefecture, central Japan (Fig. 3). This site is composed primarily of late Cretaceous biotite granite (Toki granite), the basement rock in this area. Multidisciplinary scientific studies have been implemented in the MIU project for clarifying deep geological environments, developing technologies to enhance the reliability of geological disposal of high-level-radioactive wastes (Japan Nuclear Cycle Development Institute, 2002), and investigating details of hydraulic properties of fractures and rock matrix (e.g., Koike et al., 2015; Kubo et al., 2019). Among them, geological surveys, geophysical logging, and packer tests were conducted along an N30˚E horizontal borehole (12MI33) with total length of 102 m at 500 m depth (Fig. 3); fracture, resistivity, and permeability data were obtained as shown in Fig. 4 (Tsuyuguchi et al., 2014), whose data is published and available in our study. The study site is under the groundwater table. Rocks are saturated as described earlier reports (e.g., Tsuji et al., 2017).

From borehole televiewer images, 297 fractures were observed along borehole 12MI33. The typical observed results are summarized in Fig. 4c and Table 1. The fractures generally accompany filling minerals and argillic alterations composed of chlorite and epidote (Kubo et al., 2019; Yoshida et al., 2013). The filling minerals, materials, and water decrease the fracture resistivity to below the level of the rock matrix resistivity. This decline was confirmed by the low resistivity of the water samples collected from borehole 12MI33. Fractures were concentrated in the damage zone around a minor fault that appeared in the tunnel (gallery) along 12MI33 (Fig. 3), as shown in Fig. 4c and d (Tsuyuguchi et al., 2014), whose data is published and available in our study. Only 17 fractures were observed to be open with clear apertures of about 0.5 mm (Fig. 4c). Using spherical K-means clustering, the fractures
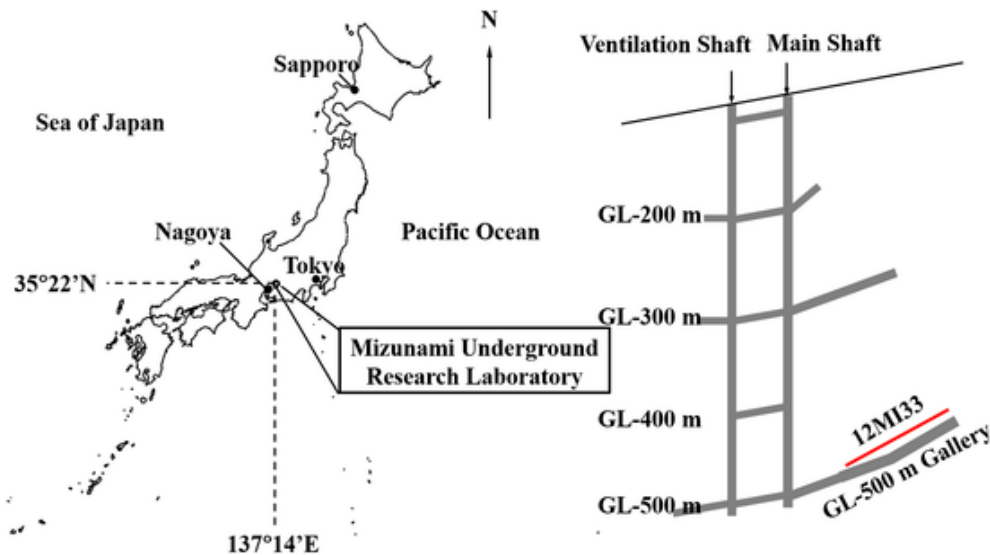
Fig. 3. Location map of the Mizunami Underground Research Laboratory and the borehole 12MI33 with 102 m length marked as a red line in the Tono area, central Japan. Geological surveys, electric logging, and hydraulic tests were implemented in 12MI33 at the 500-m-deep gallery. (For interpretation of the references to colour in this figure legend, the reader is referred to the web version of this article.)
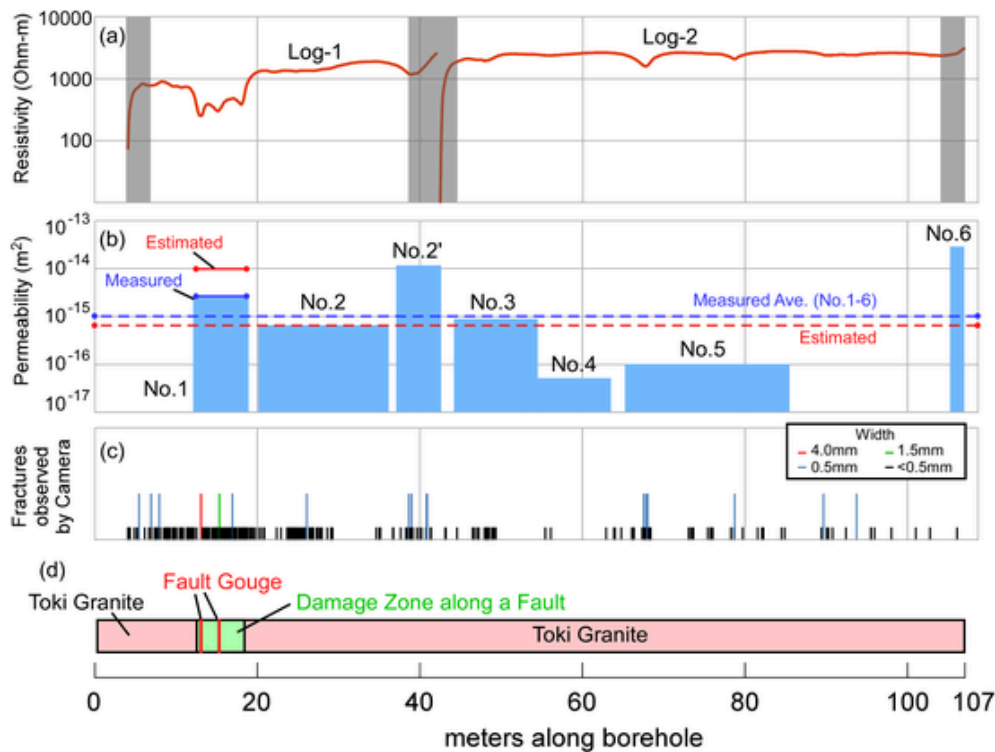

Fig. 4. Summary of observed data along the horizontal borehole 12MI33 with (a) in situ resistivity data, (b) measured permeability by hydraulic tests at the six borehole sections (Nos. 1–6), (c) distribution of fractures observed clearly by the borehole televiewer, and (d) geological settings based on descriptions of core samples. Two electric loggings (Log-1 and Log-2) were implemented. The gray hatched zones were excluded because of abnormal values in (a). Blue dashed and solid bars in (b) represent the average of all data in the six sections and in-situ measured value in the No. 1 section. Red dashed and solid bars are the permeabilities estimated using the proposed method, as described in Section 4. (For interpretation of the references to colour in this figure legend, the reader is referred to the web version of this article.)

were grouped into a single set with the average dip direction and angle shown in Table 1 (Kalinina et al., 2018). Parameter K in the von Mises–Fisher directional statistics was found as 7.0, which demonstrated that the fracture orientations are well approximated by the Fisher distribution (Kalinina et al., 2018).

These fracture parameters are used in our DFN modeling, described later. Two cases, (Table 1) are conducted: i) averaged values along borehole 12MI33, and ii) averaged ones only in the section No.1 of

12MI33. Each fracture location is not accurately modeled. Instead, the fracture distribution shown in Table 1 is used in the modeling. Fracture aperture is a critical parameter for which an adjustment is required in the DFN model. In this study, The authors simply assume the representative values of electrical and hydraulic apertures based on the borehole-based observations and experiments, then investigate how effective the adjustment of only one parameter (fracture length) of DFN generation is to reproduce the observed permeability. Fractures occur

Table 1
Observed fracture orientation and density for the DFN modeling. Cases 1 and 2 respectively denote the average fracture parameters along borehole 12MI33 and parameters only for the No. 1 section in Fig. 4. The dip direction is measured in a clockwise fashion from true north.

Case 1(Avg.)	dip (°)	dip direction (°)	κ	P_{10} (m^{-1})
set-1	82.0	28.0	7.0	0.17

Case 2 (No.1)	dip (°)	dip direction (°)	κ	P_{10} (m^{-1})
set-1	62.4	52.2	5.0	0.44

at all scales, and the multi-scale fractures would be involved in the modeling. The authors focus only on the open (visible) fractures having various fracture length in this study, since the distribution of fractures observed by the borehole televiewer and the geological settings show a good correspondence with the measured permeability values by hydraulic tests (especially at the section No. 1 and the surroundings; Fig. 4). Here, the 17 open fractures (Fig. 4c) were used for $\bar{\rho}$ by assuming that all electrical apertures are equal to the geometrical aperture 0.5 mm irrespective of the fracture length. Another important parameter is hydraulic aperture b, which differs from the geometry aperture but which can be estimated using an empirical equation derived from laboratory tests and assuming a proportional relation to the fracture radius, as described in an earlier report (Kalinina et al., 2018):

$$b = 1.16 \times 10^{-5} r \tag{15}$$

3.2. Physical properties of rock

The in-situ resistivity data by electrical logging using short normal with 25 cm electrode separation was 250–2770 Ωm along 12MI33 (Iwatsuki et al., 2019), as presented in Fig. 4a. One remarkable feature is the large decrease of resistivity in the fault damage zone (the No.1 section), with average 600 Ωm versus the overall average of 2000 Ωm. It is noteworthy that the erroneous resistivities in the hatched zones (Fig. 4b) were excluded from analyses. To assign the resistivity of the saturated fracture, the resistivity of the water samples from 12MI33 was measured as 7.0 Ωm (Table 2). The matrix resistivity without open fractures was assumed as 5000 Ωm based on the maximum resistivity measured at intact rock masses on the GL-500 m gallery (Fig. 3). Other rock properties obtained using geophysical logging were 2.56 g/cm^3 average density (2.36 g/cm^3 around the No. 1 section), 2% or less porosity, and 5.5–5.7 km/s P-wave velocity (Tsuyuguchi et al., 2014), which suggests intact granite along 12MI33, except for the damage zone.

The hydraulic conductivities K_{ij} (m/s) obtained through the hydraulic tests are portrayed in Fig. 4c, which were converted into permeability k_{ij} (m^2) by:

$$K_{ij} = \frac{\rho_w g}{\mu} k_{ij} \tag{16}$$

Table 2
Parameter values used for DFN modeling and crack tensor.

Matrix resistivity	5000 Ωm
Fracture resistivity	7.0 Ωm
Field-scale resistivity	Case 1 (Avg.): 2000 Ωm
	Case 2 (No. 1): 600 Ωm
Characteristic size	100 m
Minimum fracture length	0.5 m
Maximum fracture length	100.0 m
Side length of each grid block size	20 m as explained in 4.1.
Scaling exponent	2.5 to 3.5
Electrical aperture	5.0 × 10^{-4} m
Hydraulic aperture	Application of Eq. (15)

where μ represents fluid viscosity (1.0 × 10^{-3} Pa • s), ρ_w signifies water density (1000 kg/m^3), and g stands for gravitational acceleration (9.8 m/s^2). A value 1.0 × 10^{-15} m^2 was used as a reference field-scale permeability, similarly to a study reported by Iwatsuki et al. (2019).

3.3. Model setup

Two cases of fracture parameters were prepared for DFN modeling to examine permeable fractures specifically: Case 1 – averages of all fracture data; and Case 2 – averages of only fracture data in the highly permeable section of No. 1 (Table 1). The No. 2 section was around the junction of two logging tests: Log-1 and Log-2 (Fig. 4a). Furthermore, the No. 6 section had a high flow rate of groundwater observed at the end of drilling (Tsuyuguchi et al., 2014). Both were permeable, but they were excluded because of a lack of resistivity data. Details of all results are explained below for Case 1, but only main results are shown for Case 2.

Parameter values used for the DFN modeling and crack tensor are presented in Table 2. Cubic grid blocks of 5 × 5 × 5 with each side length (REV size) of 20 m were set in the computational domain. First, several tests were performed to decide the range of a. When a was smaller than 2.5 or larger than 3.5, the estimated electrical resistivity of a DFN model differed greatly from the in-situ measured electrical resistivity. Consequently, the optimum value of a was selected as 2.5–3.5 through matching between the calculated $\bar{\rho}$ and the resistivity data.

Three axes of the calculation domain were set along E–W (x) and N–S (y). The vertical (z) and the domain were divided into several grid blocks of cubic shape by assuming that REV was smaller than this grid-block. The authors ascertained the REV size of fractured rock mass following the method reported by Min et al. (2004). After 100 large 'parent' DFN models of 100 m × 100 m × 100 m were generated, each model was divided into grid blocks with 5–25 m side length. The average of $\bar{k}$ values of all grid blocks changed with increasing unit grid-block size. A suitable REV size was inferred when the change of $\bar{k}$ average became gradual.

4. Results

4.1. REV size

The $\bar{k}$ averages of grid blocks decreased concomitantly with increasing side block length using the maximum (3.5) and minimum (2.5) a values (Fig. 5). Both changes became gradual at a certain side length (e.g., 20 m) or greater side length. Based on Fig. 5, a larger side length would be preferable to estimate the effective permeability. However, in the crack tensor theory, the rock masses are treated as homogeneous media (Oda, 1985). The fracture distribution in the large parent DFN model is stochastically generated, and not always statistically homogeneous. That is a reason to establish the REV, in which the characteristic of fractures assumed to be constant. In addition, considering the statistical stability, a large number of grid blocks (e.g., >100) is preferable for the estimation of the $\bar{k}$ average of a DFN model.

Determination of optimal block size of a REV is a subjective task, depending the stability of estimated physical parameters and its spatial resolution (e.g., Min et al., 2004). Although several methods to determine the size of REV are proposed (Min et al., 2004; Ni et al., 2017; Ma et al., 2020), a simple way is applied here; the REV size corresponds to the minimum size beyond which the averaged physical value is stable (Pouya and Ghoreychi, 2001; Chalhoub and Pouya, 2008). The corner of curve in Fig. 5 is not sharp, so several different values represent reasonable block sizes; 19–22 m approximately. More quantitatively, the relative difference of effective permeability between two neighboring block sizes (e.g., 15 & 16 m, 16 & 17 m, and so on) is calculated. It keeps around 5%, and does not change much beyond the block size of 20 m. The authors consider the relative difference with 5% can be ac-
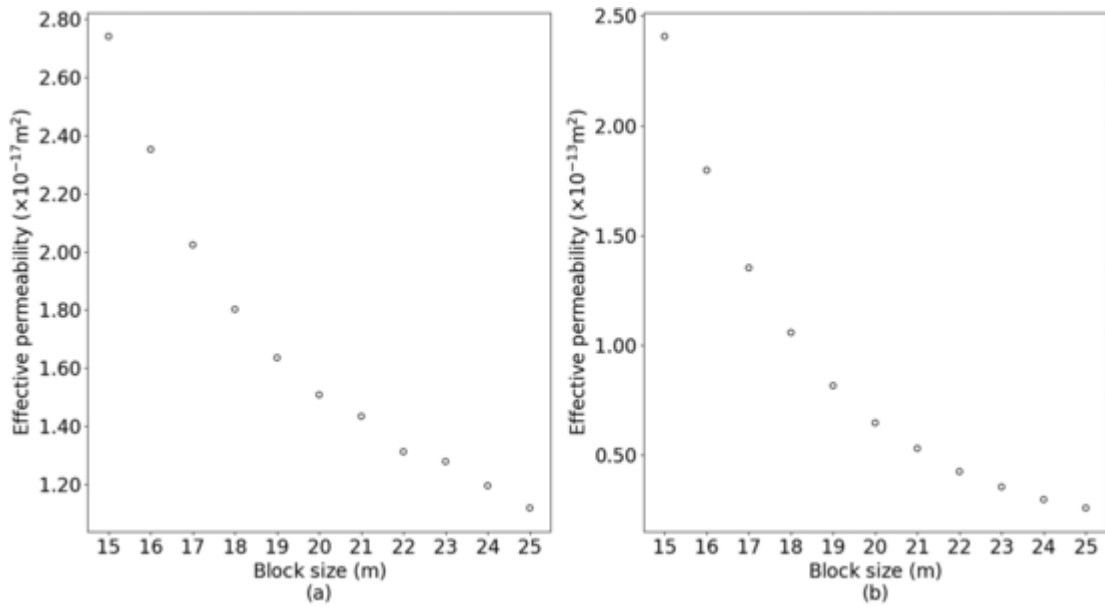
Fig. 5. Change in the average of effective permeability of grid blocks in a computational domain with 100 m characteristic side length. DFN models were constructed using the parameters defined in Tables 1 and 2 with scaling exponents a (a) 3.5 and (b) 2.5.

cepted as small. In addition, the large 'parent' DFN model has a side length of 100 m, so that the REV size is basically limited to its divisors: 10, 20, 25, or 50 m. Therefore, the REV size was determined as 20 m in the later results. Another case under the REV size of 25 m will be also discussed later.

4.2. Optimum DFN model

The scaling exponent a has a great effect on the fracture length and density, and also on the physical parameters of the rock mass (effective resistivity and permeability). The average fracture length in the DFN model for Case 1 decreased gradually with a (Fig. 6). It is easily inferred from the definition of a (see Eq. (3)). The number of fractures per unit volume in the computational domain, P_{30} (m^{-3}), increased with increas-

ing a value (Fig. 7). In this study, the constant fracture density is assumed in the DFN modeling; however, it is the number of fractures per unit length P_{10} (m^{-1}) shown in Table 1. The longer fractures contribute to P_{10} values as well as smaller fractures, but less to P_{30} values. The averages of $\bar{\rho}$ and $\bar{k}$ values of 125 grid blocks also changed gradually with increasing a value (Fig. 8). As an example of the constructed DFN model, the model with the shortest average fracture length by $a = 3.5$ is presented in Fig. 9a, for which the average $\bar{\rho}$ (3094 Ωm) is larger than the field-scale resistivity, 2000 Ωm (Table 2). The resistivity difference is much larger than the matching criterion in Fig. 2. Therefore, the DFN model is unsuitable. By repeating the change of the a value, the resistivity difference fell into the criterion at $a = 3.0$. The optimum DFN model was obtained as presented in Fig. 9b. Regarding Case 2, optimum a was found as 2.8 for average fracture length assigned as 1.10 m.
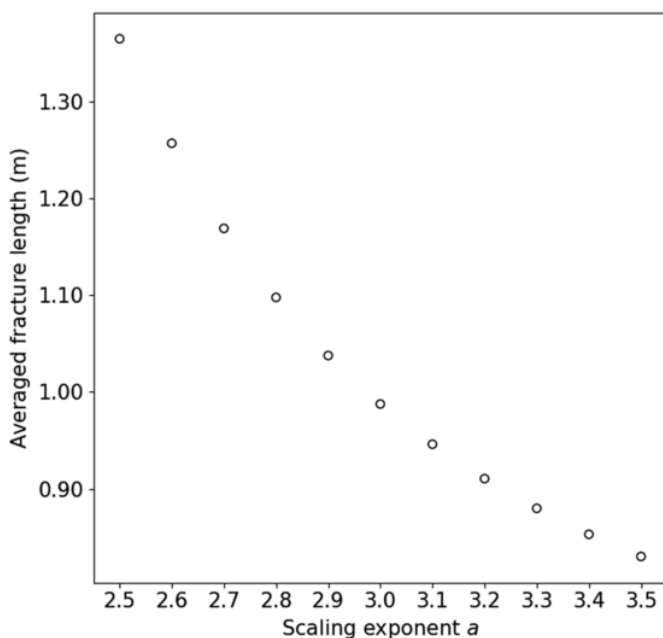

Fig. 6. Relation between average facture length and scaling exponent a between 2.5 and 3.5 for Case 1.
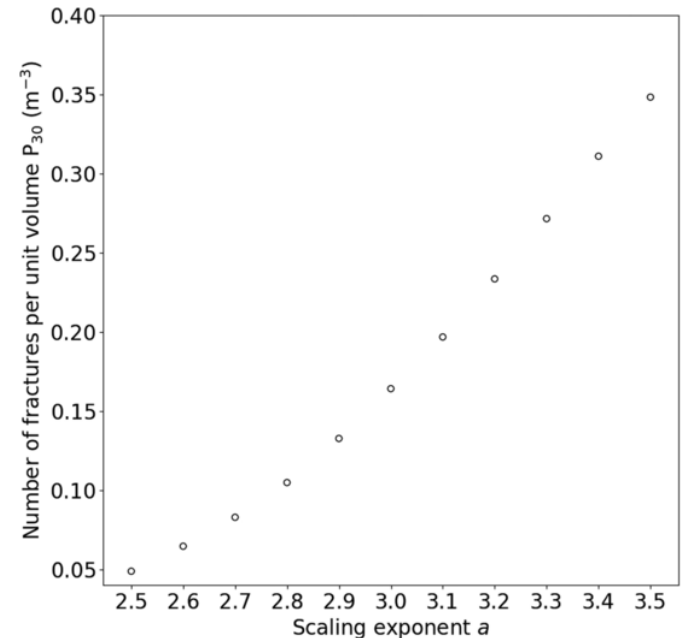

Fig. 7. Relation between the number of fractures per unit volume P_{30} and scaling exponent a between 2.5 and 3.5 for Case 1.
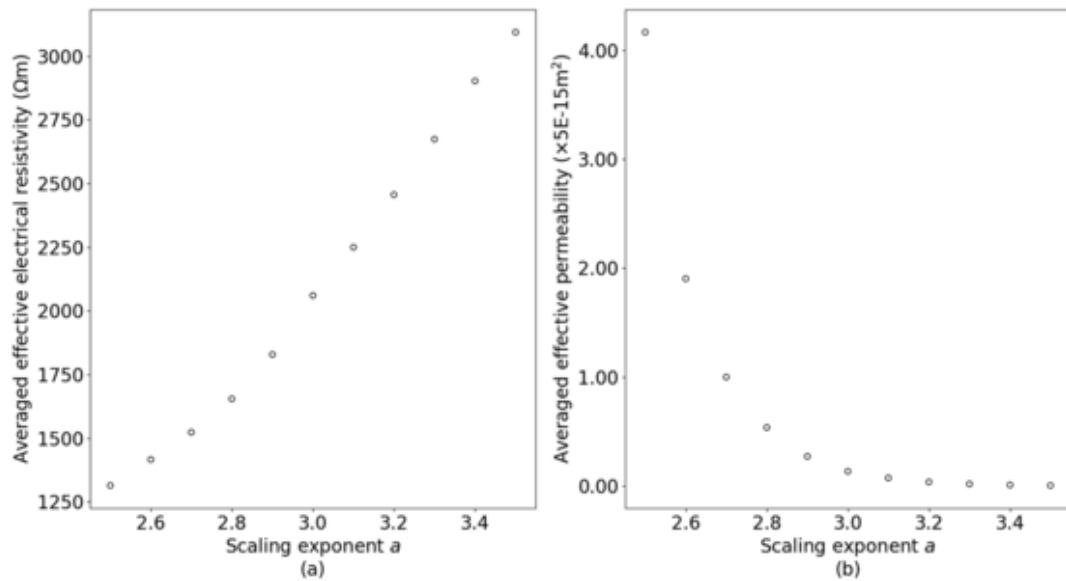
Fig. 8. Relationship between scaling exponent a (= 2.5–3.5) and (a) average of effective electrical resistivity and (b) effective permeability of 125 grid blocks, respectively for Case 1. The dashed line in (a) shows the in-situ measured resistivity value.
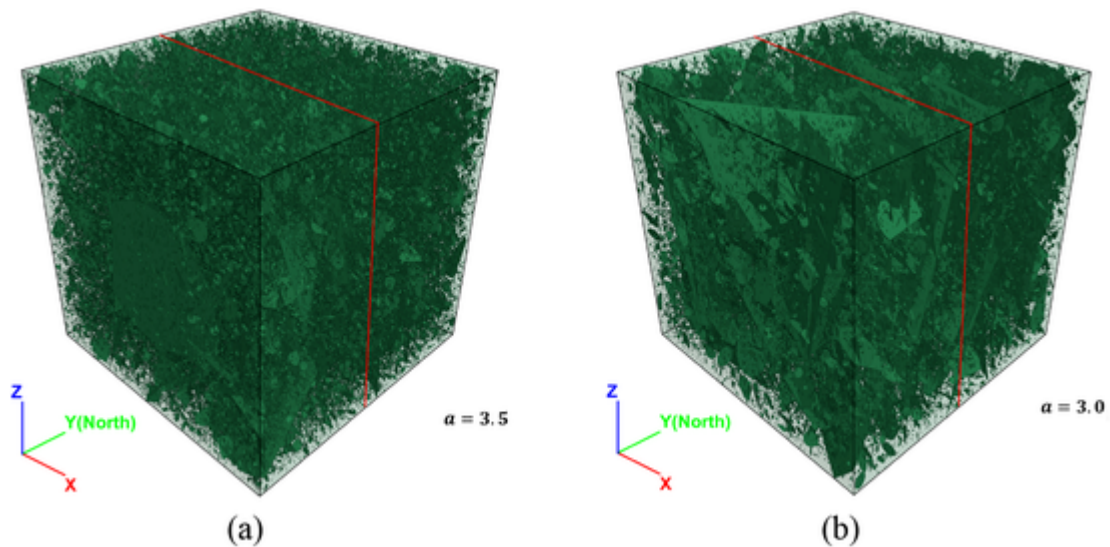

Fig. 9. DFN models constructed for Case 1 with a = 3.5 (a) and the optimum value, 3.0 (b) in the calculation domain of 100 m × 100 m × 100 m and the location of cross-sections in Fig. 10 by red lines. The (a) model does not satisfy the convergence criterion presented in Fig. 2. Finally, the (b) model is used for subsequent examinations and discussions. The x, y, and z axes are respectively oriented eastward, northward, and upward vertical. (For interpretation of the references to colour in this figure legend, the reader is referred to the web version of this article.)

Sensitivity of fracture distribution to a was demonstrated using a vertical cross-section in the middle of y axis (y = 50 m) by comparing two DFN models with a = 3.5 and 3.0 for Case 1 (Fig. 10). The respective average fracture lengths are 0.83 m (a = 3.5) and 0.99 m (a = 3.5). Comparison confirms the presence of many more long fractures in the model a = 3.0, which almost matched the calculated $\overline{\rho}$ almost with the measured resistivity. Results show that the constraint of resistivity data obtained from geophysical logging is valid for construction of a plausible DFN model.

4.3. Effective electrical resistivity

The ρ_{ij} values along the x, y, and z axes of each grid block in the DFN model with a = 3.0 are presented in Fig. 11. The resistivity along each direction differs because of anisotropy of the DFN model (Fig. 9b). However, $\overline{\rho}$ was 2064 Ωm, which is around the field-scale resistivity of 2000 Ωm. This similarity also supports the suitability of the DFN model.

4.4. Effective permeability

The diagonal permeability components, k_{xx}, k_{yy}, and k_{zz} of each grid block in the DFN model with a = 3.0 and their planar distributions at the vertical cross-section as the same location with Fig. 10 are depicted respectively in Figs. 12 and 13. Grid blocks with high permeabilities in Fig. 12 correspond to small resistivities in Fig. 11. Averages of all k_{xx}, k_{yy}, and k_{zz} values and the resultant $\overline{k}$ are compared with the hydraulic test data in Table 3. Because the fractures were steep, as shown by the average dip, 82° (Table 1), a feature by which k_{zz} (related to vertical flow) and k_{yy} (related to horizontal flow) are, respectively, the maximum and minimum, is reasonable. The second largest value of k_{xx} is related to the dominant strike of fractures, N62°W, which is perpendicu-
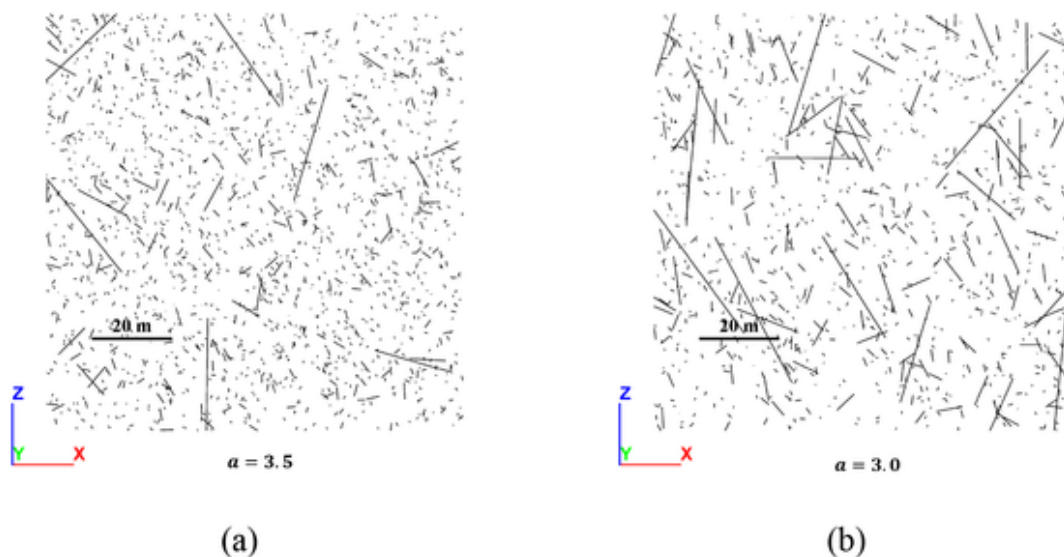
Fig. 10. Vertical cross-sections of the DFN models in Fig. 9, constructed with $a = 3.5$ (a) and 3.0 (b), at the middle of the y axis ($y = 50$ m).
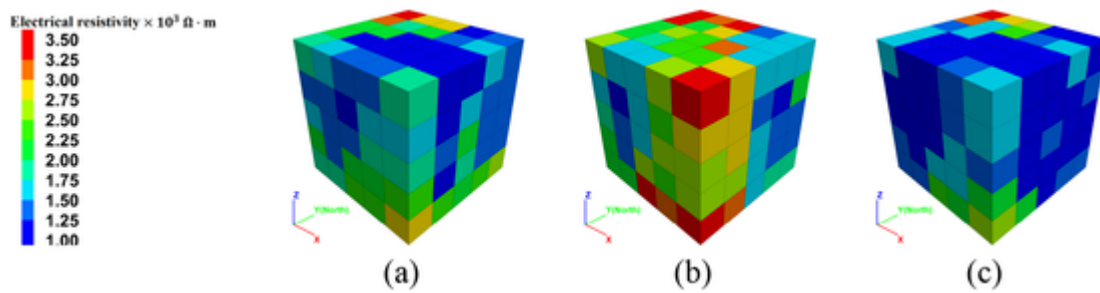

Fig. 11. Resistivities of diagonal components, (a) ρ_{xx}, (b) ρ_{yy}, and (c) ρ_{zz} of respective DFN model grid blocks constructed with $a = 3.0$ for Case 1 in Fig. 9b. The side length of each grid block is 20 m. The calculation domain size is shown in Fig. 9.
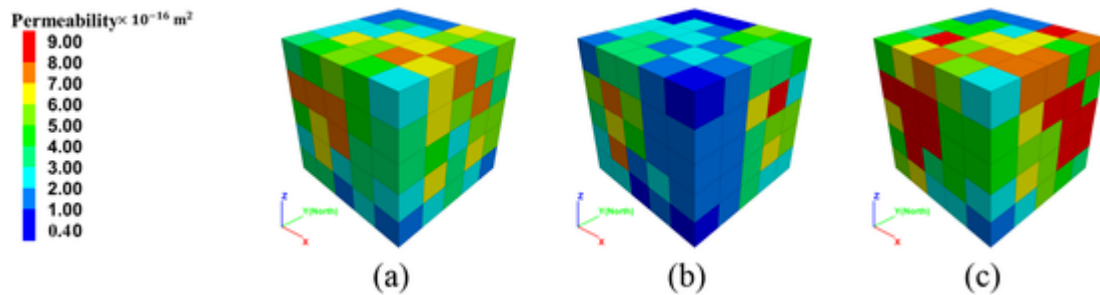

Fig. 12. Permeabilities of diagonal components, (a) k_{xx}, (b) k_{yy}, and (c) k_{zz} of each grid blocks in the DFN model constructed with $a = 3.0$ for Case 1 in Fig. 9b. The domain size is presented in Fig. 11.
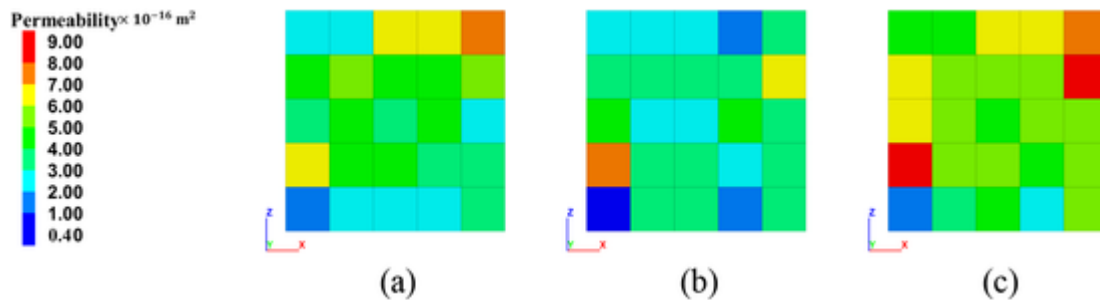

Fig. 13. Vertical cross-sections of (a) k_{xx}, (b) k_{yy}, and (c) k_{zz} of grid blocks in the DFN model constructed with $a = 3.0$ for Case 1 in Fig. 12. The cross-section location is portrayed in Fig. 10.

Table 3
Comparison between calculated diagonal permeabilities through the constructed DFN model in Fig. 9b and permeability by in-situ hydraulic testing.

Case 1 (Avg.)	Calculated effective permeability (m²)	In-situ measured permeability (m²)
k_{xx}	7.36×10^{-16}	Unmeasured
k_{yy}	3.98×10^{-16}	Unmeasured
k_{zz}	8.60×10^{-16}	Unmeasured
$\frac{1}{3}(k_{xx} + k_{yy} + k_{zz})$	6.65×10^{-16}	1.0×10^{-15}

Case 2 (No. 1)	Calculated effective permeability (m²)	In-situ measured permeability (m²)
k_{xx}	9.03×10^{-15}	Unmeasured
k_{yy}	1.07×10^{-14}	Unmeasured
k_{zz}	1.13×10^{-14}	Unmeasured
$\frac{1}{3}(k_{xx} + k_{yy} + k_{zz})$	1.03×10^{-14}	2.67×10^{-15}

lar to the main dip direction, 28° (Table 1). Comparison of Figs. 10 and 12 reveals that the k_{zz} values tend to increase in zones where long fractures are concentrated.

For the measured $\bar{k} = 1.0 \times 10^{-15}$ m², the value of $\bar{k}$ calculated using the proposed method was about its half, 6.65×10^{-16} m². The calculated $\bar{k}$ in Case 2, 1.03×10^{-14} m², was about four times larger than the measured $\bar{k} = 2.67 \times 10^{-15}$ m² (Table 3). Despite these discrepancies, the differences are smaller than one order in both cases. Therefore, the proposed method can be regarded as effective.

5. Discussion

In this study, the difference between the calculated effective permeability and in-situ measured permeability is less than one order for each case. The authors believe that our scheme of permeability estimation is effective; however, minor difference still remains. One possible cause of the difference is the presence of clay minerals as filling fractures: chloritization was observed in the fault gouge in the core samples from damage zone from the No. 1 section (Fig. 4; Tsuyuguchi et al., 2014). Clay minerals in saturated rocks generally decrease the resistivity and permeability. If clay minerals are not taken into consideration, the lower the resistivity, the longer the fracture length (which may result in the over-estimation of permeability). Accordingly, the predicted $\bar{k}$ was slightly higher than the actual value at the No. 1 section (Case 2 in Table 3; Fig. 4b). Another possible cause is that a single-borehole hydraulic test was unable to measure anisotropic permeabilities of fractured rock mass: the in-situ measured permeability is always an average behavior, irrespective of direction. Fractures perpendicular to the borehole direction tend to appear much more than fractures parallel to the direction. This directional bias of fractures might induce a phenomenon by which the measured permeability differs from the intrinsic permeability of the fractured rock mass.

This study optimized only one unknown parameter a, scaling exponent, in the DFN model. Other parameters such as fracture location and aperture are also necessarily constrained to construct a more accurate DFN model using data of various types. A multi-parameter optimization scheme is expected to be effective for the constraint. Then, multiple DFN models with equal accuracy might be built. Geophysical logging tool (Fig. 1) obtains various physical parameters along a borehole (e.g., seismic velocity, density, porosity with resistivity), and will be helpful for the multi-parameter optimization. Several other approaches can be also used to reduce uncertainty of DFN models. For example, microseismic data together with geologic data were used to constrain fracture locations to decrease uncertainty of the DFN models (Sun et al., 2016). In this method, fracture length was assumed to follow a power-law distribution without any constraint and only fracture locations were con-

strained by considering that microseismic events were located at or close to fractures. Instead of constraining fracture locations of a DFN model, the power law parameters in DFN models were calibrated using in-situ hydrogeological data (Follin et al., 2014) with construction of initial DFN model using the geological data obtained from the boreholes. The frequency of connected open fractures observed in the hydraulic pumping tests was used to adjust the size distributions of fractures. Those two approaches can be implemented to reduce the uncertainties of DFN models by using available datasets (e.g., geophysical logging and hydraulic tests along a test borehole), then the optimized model parameters can be applied to permeability prediction along other boreholes. Even with our limited parameter optimization, the estimated permeability along borehole 12MI33 is similar to the observed ones with moderately small discrepancies (less than one order of magnitude; Cases 1 and 2 in Table 3). As mentioned, electrical resistivity was selected by this study to constrain a DFN model because of its sensitivity to fractures. Geophysical surveys for in-situ electrical resistivity data are common in engineering practice (e.g., tunnel construction). Consequently, using electrical resistivity data as a constraint of building a DFN model is feasible, and a permeability of fractured rock is obtainable.

Several issues remain in relation to our proposed method. The effective permeability continues to decrease over the side length of the DFN model, 20 m, although the rate of decrease becomes low as shown in Fig. 5. This phenomenon may result from the relation between hydraulic aperture and the fracture length. Effective permeability becomes constant over a certain block size if the hydraulic aperture is constant and does not vary with the fracture length. To check suitability of the REV size of 20 m for estimating the effective permeability, the side length was changed to 25 m and the values of $\bar{k}$ were calculated by using $a = 2.5$–3.5 for Case 1. As shown in Fig. 14, the difference of $\bar{k}$ between the two side lengths is small in the a range 2.9–3.5, whereas the difference becomes large for a smaller than 2.7. It is probable therefore that the effect of the REV size on $\bar{k}$ is small in the range of $a = 2.7$–3.5. Although the difference of $\bar{k}$ becomes large with decreasing a from 2.7 and maximizes at $a = 2.5$, the relative difference is 20% at most. Consequently, the 20 m size is proper to evaluate the effective permeability for $a = 2.5$–3.5. One caution is that larger REV size may produce
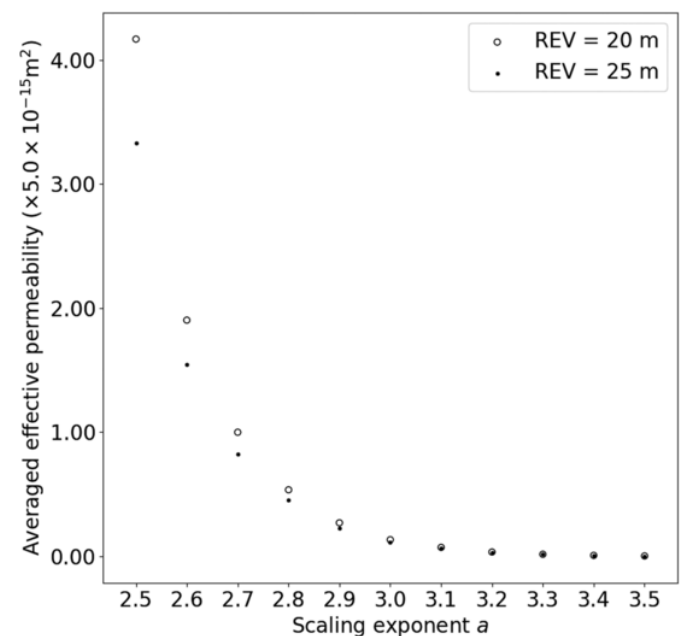

Fig. 14. Relation between average of effective permeability of grid blocks and a between 2.5 and 3.5 for Case 1 with two REV sizes of 20 m and 25 m.

slightly smaller effective permeability, because $\bar{k}$ of the REV size 25 m is smaller than $\bar{k}$ of 20 m (Fig. 14).

The authors used effective permeability in this study to represent fractured rock permeability. Using equivalent permeability is also possible. This equivalent permeability does not necessarily require a REV size of DFN model, which seems more flexible than the effective permeability. However, equivalent permeability is changeable with the gridblock size. Accordingly, several equivalent permeabilities might be calculated under a condition for determining a single effective permeability, which results in increasing uncertainty of permeability estimation. Although more examination of the difference between effective and equivalent permeabilities is necessary, effective permeability might be suitable for a comparison with the in-situ measured permeability.

6. Conclusion

This study was conducted using resistivity logging data obtained in pilot drilling for tunnel excavation as a constraint of the distribution, thereby overcoming a persistent difficulty of DFN modeling: uncertainty in fracture length distribution. Effectiveness of using the electrical resistivity and the symmetric self-consistent method were proved respectively to constrain fracture lengths and calculate electrical resistivity of a DFN model. Through this application, an optimized scaling exponent for the fracture distribution was determined, which enabled derivation of a suitable effective permeability of the x, y, and z axes and their average using an improved Oda's crack tensor theory.

To validate the proposed method, we conducted two case studies examining fracture and resistivity data obtained from a borehole at 500 m depth at the Mizunami Underground Research Laboratory, central Japan. The data were from the Toki granite. The difference between the average effective permeability using our proposed method and the averaged permeability measured by hydraulic tests was less than one order. For Case 1, which targeted the whole case study area with all available data, a DFN model with scaling exponent $a = 3.5$ was unsuitable, because its $\bar{\rho}$ was larger than the in-situ measured resistivity. By changing a to 3.0, the optimal DFN model was constructed with corresponding average effective permeability $\bar{k} = 6.5 \times 10^{-16}$ m², which is about half of in-situ measured permeability 1.0×10^{-15} m². For Case 2, which was limited to the fault damage zone, a was set as 2.8. The calculated $\bar{k}$ was 1.03×10^{-14} m², which was about four times greater than the in-situ measured permeability of 2.67×10^{-15} m². Based on results of these two case studies, we conclude that the constrained DFN modeling approach using in-situ resistivity data can avoid constructing unrealistic DFN models with too many short fractures.

Improvement of the proposed method, our next step, can be accomplished by changing the Oda's crack tensor theory and the symmetric self-consistent method, which are empirical methods, to more accurate numerically based methods. Moreover, this study examined only the effects of a on the DFN modeling, but the modeling accuracy depends also on other parameters such as the minimum and maximum fracture lengths, fracture aperture, fracture location together with clay mineral contents. Deep consideration of all control parameters for DFN modeling and their sensitivities to the accuracy of DFN models will be achieved by multi-physical data, and are important subjects for future work.

CRediT authorship contribution statement

Jin Wu: Conceptualization, Methodology, Software, Formal analysis, Visualization, Writing - original draft. **Tada-nori Goto:** Investigation, Visualization, Writing - review & editing, Project administration, Funding acquisition. **Katsuaki Koike:** Supervision, Writing - review & editing, Funding acquisition.

Declaration of Competing Interest

The authors declare that they have no known competing financial interests or personal relationships that could have appeared to influence the work reported in this paper.

References

Barenblatt, G., Zheltov, I., Kochina, I., 1960. Basic concepts in the theory of seepage of homogeneous liquids in fissured rocks [strata]. J. Appl. Math. Mech. 24, 1286–1303. https://doi.org/10.1016/0021-8928(60)90107-6.

Chalhoub, M., Pouya, A., 2008. Numerical homogenization of a fractured rock mass: a geometrical approach to determine the mechanical representative elementary volume. Electron. J. Geotech. Eng. 13, 1–12.

den Boer, Sayers, C.M., 2018. Constructing a discrete fracture network constrained by seismic inversion data. Geophysical Prospecting 66 (1), 124–140.

Dershowitz, W.S., Einstein, H.H., 1988. Characterizing rock joint geometry with joint system models. Rock Mech. Rock. Eng. 21, 21–51. https://doi.org/10.1007/BF01019674.

Dershowitz, W.S., Fidelibus, C., 1999. Derivation of equivalent pipe network analogues for three-dimensional discrete fracture networks by the boundary element method. Water Resour. Res. 35, 2685–2691. https://doi.org/10.1029/1999WR900118.

Dorn, C., Linde, N., Le Borgne, T., Bour, O., de Dreuzy, J.-R., 2013. Conditioning of stochastic 3-D fracture networks to hydrological and geophysical data. Adv. Water Resour. 62, 79–89. https://doi.org/10.1016/J.ADVWATRES.2013.10.005.

Follin, S., Hartley, L., Rhén, I., Jackson, P., Joyce, S., Roberts, D., Swift, B., 2014. A methodology to constrain the parameters of a hydrogeological discrete fracture network model for sparsely fractured crystalline rock, exemplified by data from the proposed high-level nuclear waste repository site at Forsmark, Sweden. Hydrogeol. J. 22, 313–331. https://doi.org/10.1007/s10040-013-1080-2.

Hadgu, T., Karra, S., Kalinina, E., Makedonska, N., Hyman, J.D., Klise, K., Viswanathan, H.S., Wang, Y., 2017. A comparative study of discrete fracture network and equivalent continuum models for simulating flow and transport in the far field of a hypothetical nuclear waste repository in crystalline host rock. J. Hydrol. 553, 59–70. https://doi.org/10.1016/j.jhydrol.2017.07.046.

Hamm, S.Y., Kim, M.S., Cheong, J.Y., Kim, J.Y., Son, M., Kim, T.W., 2007. Relationship between hydraulic conductivity and fracture properties estimated from packer tests and borehole data in a fractured granite. Eng. Geol. 92, 73–87. https://doi.org/10.1016/j.enggeo.2007.03.010.

Ishibashi, M., Yoshida, H., Sasao, E., Yuguchi, T., 2016. Long term behavior of hydrogeological structures associated with faulting: An example from the deep crystalline rock in the Mizunami URL. Central Japan. Eng. Geol. 208, 114–127. https://doi.org/10.1016/J.ENGGEO.2016.04.026.

T. Iwatsuki H. Onoe M. Ishibashi DECOVALEX-2019 Task C; GREET Intermediate Report [WWW Document] URL https://jopss.jaea.go.jp/search/servlet/search?5064318&language=1 2019 (accessed 3.23.20)

Japan Nuclear Cycle Development Institute, 2002. Master Plan of the Mizunami Underground Research Laboratory Project, JNC-TN7410 2003-001. 153 pp..

Kalinina, E., Hadgu, T., Wang, Y., Ozaki, Y., Iwatsuki, T., 2018. Development and validation of a fracture model for the granite rocks at Mizunami underground research laboratory Japan. In: Proceeding of 2nd International Discrete Fracture Network Engineering Conference, DFNE18-435. American Rock Mechanics Association.

Karimi-Fard, M., Durlofsky, L.J., Aziz, K., 2003. An Efficient Discrete Fracture Model Applicable for General Purpose Reservoir Simulators, in: SPE Reservoir Simulation Symposium. Society of Petroleum Engineers. https://doi.org/10.2118/79699-MS.

Koike, K., Liu, C., Sanga, T., 2012. Incorporation of fracture directions into 3D geostatistical methods for a rock fracture system. Environ. Earth Sci. 66, 1403–1414. https://doi.org/10.1007/s12665-011-1350-z.

Koike, K., Kubo, T., Liu, C., Masoud, A., Amano, K., Kurihara, A., Matsuoka, T., Lanyon, B., 2015. 3D geostatistical modeling of fracture system in a granitic massif to characterize hydraulic properties and fracture distribution. Tectonophysics 660, 1–16. https://doi.org/10.1016/J.TECTO.2015.06.008.

Kubo, T., Matsuda, N., Kashiwaya, K., Koike, K., Ishibashi, M., Tsuruta, T., Matsuoka, T., Sasao, E., Lanyon, G.W., 2019. Characterizing the permeability of drillhole core samples of Toki granite, Central Japan to identify factors influencing rock-matrix permeability. Eng. Geol. 259, 105163. https://doi.org/10.1016/J.ENGGEO.2019.105163.

Lei, Q., Latham, J.-P., Xiang, J., Tsang, C.-F., Lang, P., Guo, L., 2014. Effects of geomechanical changes on the validity of a discrete fracture network representation of a realistic two-dimensional fractured rock. Int. J. Rock Mech. Min. Sci. 70, 507–523. https://doi.org/10.1016/J.IJRMMS.2014.06.001.

Lei, Q., Latham, J.-P., Tsang, C.-F., 2017. The use of discrete fracture networks for modelling coupled geomechanical and hydrological behaviour of fractured rocks. Comput. Geotech. 85, 151–176. https://doi.org/10.1016/J.COMPGEO.2016.12.024.

Leung, C.T.O., Hoch, A.R., Zimmerman, R.W., 2012. Comparison of discrete fracture network and equivalent continuum simulations of fluid flow through two-dimensional fracture networks for the DECOVALEX–2011 project. Mineral. Mag. 76, 3179–3190. https://doi.org/10.1180/minmag.2012.076.8.31.

Li, J.H., Zhang, L.M., Wang, Y., Fredlund, D.G., 2009. Permeability tensor and representative elementary volume of saturated cracked soil. Can. Geotech. J. 46, 928–942. https://doi.org/10.1139/T09-037.

Liu, C., Kubo, T., Lu, L., Koike, K., Zhu, W., 2019. Spatial simulation and characterization of three-dimensional fractures in Gejiu tin District, Southwest China, using GEOFRAC. Nat. Resour. Res. 28, 99–108. https://doi.org/10.1007/s11053-018-9381-8.

Ma, K., Wang, L., Peng, Y., Long, L., Wang, S., Chen, T., 2020. Permeability characteristics of fractured rock mass: a case study of the Dongjiahe coal mine. Geomat. Nat. Hazards Risk 11, 1724–1742. https://doi.org/10.1080/19475705.2020.1811403.

Mak, S.W., 2014. Assessing fracture network connectivity of prefeasibility-level high temperature geothermal projects using discrete fracture network modelling. https://doi.org/10.14288/1.0167612.

Min, K.-B., Jing, L., Stephansson, O., 2004. Determining the equivalent permeability tensor for fractured rock masses using a stochastic REV approach: Method and application to the field data from Sellafield, UK. Hydrogeol. J. 12, 497–510. https://doi.org/10.1007/s10040-004-0331-7.

Mourzenko, V.V., Thovert, J.F., Adler, P.M., 2011. Permeability of isotropic and anisotropic fracture networks, from the percolation threshold to very large densities. Phys. Rev. E - Stat. Nonlinear Soft Matter. Phys. 84, 36307. https://doi.org/10.1103/PhysRevE.84.036307.

Ni, P., Wang, S., Wang, C., Zhang, S., 2017. Estimation of REV size for fractured rock mass based on damage coefficient. Rock Mech. Rock. Eng. 50, 555–570. https://doi.org/10.1007/s00603-016-1122-x.

Oda, M., 1985. Permeability tensor for discontinuous rock masses. Geotechnique 35 (4), 483–495.

Oda, M., 1986. An equivalent continuum model for coupled stress and fluid flow analysis in jointed rock masses. Water Resour. Res. 22, 1845–1856. https://doi.org/10.1029/WR022i013p01845.

Pouya, A., Ghoreychi, M., 2001. Determination of rock mass strength properties by homogenization. Int. J. Numer. Anal. Methods Geomech. 25, 1285–1303. https://doi.org/10.1002/nag.176.

Pruess, K., Narasimhan, T., 1982. A practical method for modeling fluid and heat flow in fractured porous media. In: 6th SPE Symposium on Reservoir Simulation. Society of Petroleum Engineers. https://escholarship.org/content/qt0km6n7qv/qt0km6n7qv.pdf (accessed 3.23.20).

Pruess, K., Oldenburg, C.M., Moridis, G.J., 1999. TOUGH2 User's Guide Version 2. Lawrence Berkeley National Laboratory 197 pp..

Renard, P., De Marsily, G., 1997. Calculating equivalent permeability: a review. Adv. Water Resour. 20, 253–278. https://doi.org/10.1016/s0309-1708(96)00050-4.

Rutqvist, J., Leung, C., Hoch, A., Wang, Y., Wang, Z., 2013. Linked multicontinuum and crack tensor approach for modeling of coupled geomechanics, fluid flow and transport in fractured rock. J. Rock Mech. Geotech. Eng. 5, 18–31. https://doi.org/10.1016/j.jrmge.2012.08.001.

Sævik, P.N., Nixon, C.W., 2017. Inclusion of topological measurements into analytic estimates of effective permeability in fractured media. Water Resour. Res. 53, 9424–9443. https://doi.org/10.1002/2017WR020943.

Sævik, P.N., Berre, I., Jakobsen, M., Lien, M., 2013. A 3D computational study of effective medium methods applied to fractured media. Transp. Porous Media 100, 115–142. https://doi.org/10.1007/s11242-013-0208-0.

Sævik, P.N., Jakobsen, M., Lien, M., Berre, I., 2014. Anisotropic effective conductivity in fractured rocks by explicit effective medium methods. Geophys. Prospect. 62, 1297–1314. https://doi.org/10.1111/1365-2478.12173.

Sandve, T.H., Berre, I., Nordbotten, J.M., 2012. An efficient multi-point flux approximation method for Discrete Fracture–Matrix simulations. J. Comput. Phys. 231, 3784–3800. https://doi.org/10.1016/J.JCP.2012.01.023.

Sun, J., Gamboa, E.S., Schechter, D., Rui, Z., 2016. An integrated workflow for characterization and simulation of complex fracture networks utilizing microseismic and horizontal core data. J. Nat. Gas Sci. Eng. 34, 1347–1360. https://doi.org/10.1016/j.jngse.2016.08.024.

Tsuji, M., Kobayashi, S., Mikake, S., Sato, T., Matsui, H., 2017. Post-grouting experiences for reducing groundwater inflow at 500 m depth of the Mizunami underground research laboratory, Japan. In: Procedia Engineering. Elsevier Ltd, pp. 543–550. https://doi.org/10.1016/j.proeng.2017.05.216.

Tsuyuguchi, K., Kuroiwa, H., Kawamoto, K., Yamada, N., 2014. Results of pilot borehole investigation in -500m access/research gallery-north (12MI27 and 12MI33 boreholes). In: JAEA-Technology 2013-044. Japan Atomic Energy Agency 89 pp. https://doi.org/10.11484/jaea-technology-2013-044.

Valera, M., Guo, Z., Kelly, P., Matz, S., Cantu, V.A., Percus, A.G., Hyman, J.D., Srinivasan, G., Viswanathan, H.S., 2017. Machine learning for graph-based representations of three-dimensional discrete fracture networks. Comput. Geosci. 22, 695–710. https://doi.org/10.1007/s10596-018-9720-1.

Vogel, T., Gerke, H.H., Zhang, R., Van Genuchten, M.T., 2000. Modeling flow and transport in a two-dimensional dual-permeability system with spatially variable hydraulic properties. J. Hydrol. 238, 78–89. https://doi.org/10.1016/S0022-1694(00)00327-9.

Wang, Z., Rutqvist, J., Wang, Y., Leung, C., Hoch, A., Dai, Y., 2014. The effect of stress on flow and transport in fractured rock masses using an extended multiple interacting continua method with crack tensor theory. In: Nuclear Technology. Taylor & Francis, pp. 158–168. https://doi.org/10.13182/NT13-76.

Warren, J.E., Root, P.J., 1963. The behavior of naturally fractured reservoirs. Soc. Pet. Eng. J. 3, 245–255. https://doi.org/10.2118/426-PA.

Williams-Stroud, S., Ozgen, C., Billingsley, R.L., 2013. Microseismicity-constrained discrete fracture network models for stimulated reservoir simulation. Geophysics 78, B37–B47. https://doi.org/10.1190/geo2011-0061.1.

Wolfsberg, A., 1996. Rock Fractures and Fluid Flow: Contemporary Understanding and Applications. The National Academies Press 568 pp. https://doi.org/10.17226/2309.

Xu, C., Dowd, P., 2010. A new computer code for discrete fracture network modelling. Comput. Geosci. 36, 292–301. https://doi.org/10.1016/j.cageo.2009.05.012.

Yoshida, H., Metcalfe, R., Ishibashi, M., Minami, M., 2013. Long-term stability of fracture systems and their behaviour as flow paths in uplifting granitic rocks from the Japanese orogenic field. Geofluids 13, 45–55. https://doi.org/10.1111/gfl.12008.